Received: 3 August 2022 | Revised: 8 December 2022 | Accepted: 16 January 2023

DOI: 10.1002/sia.7193

RESEARCH ARTICLE

SURFACE and INTERFACE ANALYSIS WILEY

XPS study of the thermal stability of passivated NiCrFeCoMo multi-principal element alloy surfaces

Xueying Wang[1] | Dimitri Mercier[1] | Sandrine Zanna[1] | Antoine Seyeux[1] | Loïc Perriere[2] | Mathilde Laurent-Brocq[2] | Ivan Guillot[2] | Vincent Maurice[1] | Philippe Marcus[1]

[1]PSL Research University, CNRS - Chimie ParisTech, Institut de Recherche de Chimie Paris, Physical Chemistry of Surfaces Group, 11 rue Pierre et Marie Curie, Paris, France

[2]Université Paris Est Creteil, CNRS, ICMPE, UMR7182, Thiais, France

Correspondence
Dimitri Mercier and Philippe Marcus, PSL Research University, CNRS - Chimie ParisTech, Institut de Recherche de Chimie Paris, Physical Chemistry of Surfaces Group, 11 rue Pierre et Marie Curie, Paris 75005, France.
Email: dimitri.mercier@chimieparistech.psl.eu and philippe.marcus@chimieparistech.psl.eu

Funding information
H2020 European Research Council, Grant/Award Number: 741123

X-ray photoelectron spectroscopy analysis was applied to investigate the thermal stability under ultra-high vacuum environment of the surface oxide film formed by electrochemical passivation of a newly designed $Cr_{15}Fe_{10}Co_5Ni_{60}Mo_{10}$ (at.%) multi-principal element alloy and providing the alloy superior localized corrosion resistance compared to conventional stainless steels and alloys. A spectral decomposition methodology involving the subtraction of Auger peaks overlapping the Fe 2p and Co 2p core level regions was applied for quantification of the oxide film composition and thickness. The results show that, at 100°C, the passive oxide film is mainly dehydrated and dehydroxylated. Obvious loss of Ni hydroxide and conversion of Mo (VI) to Mo (IV) species are observed at 200°C, with further reduction of Mo species to Mo (III) observed at 300°C. In this temperature range, the total cation quantity in the oxide film remains stable despite the compositional alteration. At 400°C, Cr (III) oxide forms at the expense of Fe and Mo oxides, resulting in an oxide film essentially consisting of chromium oxide. At 500°C, Cr (III) oxide is eliminated, making the passive film unstable at this temperature. Possible Cr oxide removal mechanisms are discussed.

KEYWORDS
CrFeCoNiMo, multi-principal element alloy, passive oxide film, thermal stability, XPS

1 | INTRODUCTION

Unlike conventional alloys composed of one major element and one or more minor elements modulating the alloy properties, multi-principal element alloys (MPEA), first manufactured in 2004,[1,2] are composed of at least two major elements and contain more than three elements in total.[3] The innovative alloying strategy of MPEAs, based on a predictive computational thermodynamic approach, opens up a wide and unexplored phase and composition space, which represents enormous potential for optimizing desired properties. Enhanced corrosion resistance is one of the properties being searched for.[4–8]

Cr-containing alloys are prime examples of stainless alloys that self-protect against corrosion by virtue of surface formation of a passive oxide film.[9–11] This protective oxide film has been extensively studied using diverse surface analytical techniques such as XPS, AES, ToF-SIMS, and STM.[10–17] For conventional Cr-containing stainless steels and Ni-based alloys, it is generally accepted that the passive oxide films formed under atmospheric conditions are only a few nanometers in thickness and have a bilayer structure, with the inner oxide layer mainly composed of Cr oxide, ensuring the protective character.[11,12,16,18,19] It has also been suggested that, instead of stoichiometric oxides, the species in the oxide film may exist under non-stoichiometric form due to nonequilibrium solute capture.[20–22] The addition of Mo to Cr-containing alloys is well known to stabilize passivity and enhance the localized corrosion resistance. Mechanisms such as impeding the penetration of aggressive ions,[23,24] stabilizing the oxide

components,[25–27] and removing adsorbed sulfur[26,28] have been proposed and are still debated. In the case of MPEAs, the literature concerning passive oxide film composition is less abundant but a stratified in-depth distribution of the alloying elements in the oxide films formed on the CoCrFeMnNi Cantor alloy and $CrFeCoNiMo_x$ alloys,[14,29] and a non-equilibrium, non-stoichiometric solid solution state oxide film formed on a NiCrFeRuMoW alloy[13] have been reported.

Great efforts have been undertaken to study the stability of passive oxide films in various environments in order to extend the range of applications of self-protected alloys. Regarding thermal stability, many works addressed the behavior of the surface oxide film formed on conventional alloys upon heating under reducing, oxidizing, or humid conditions for practical applications.[30–34] Some works also focused on the heating-induced alteration of the surface oxide film under inert gas atmosphere[35] or vacuum (technically low pressures)[36–38] in order to provide basic insight into the thermal stability of the oxide components, which is crucial for further understanding the behavior of oxide films upon heating in a specific environment.[39,40] As for surface oxide films formed on MPEAs, such investigations are still lacking. Most of the relevant works focused on the oxidation resistance at high temperature in oxidizing atmospheres,[41–44] while investigation of the thermal stability of the passive oxide films is still in its infancy.[40]

In this work, we committed to investigate the thermal stability of the highly protective passive oxide films providing enhanced localized corrosion resistance to some newly-designed CrFeCoNiMo MPEAs. Such work is a prerequisite needed for interrogating the oxide growth and ion transport mechanisms in such protective oxide films via high-temperature reoxidation experiments. These new MPEAs were designed using the CALPHAD approach and manufactured to verify whether a much more corrosion-resistant CrFeCoNiMo MPEA could be obtained by elevating the Mo content[26,45] while ensuring the structural and compositional homogeneity of the alloy.[46,47] The thermodynamic modeling, the electrochemical investigations demonstrating enhanced passivity, and the characterization of the passive oxide films formed at room temperature are reported elsewhere.[48,49]

Here, we report the XPS investigation of the modifications brought by thermal heating under ultra-high vacuum (UHV) environment of the passive oxide film formed electrochemically on the $Cr_{15}Fe_{10}Co_5Ni_{60}Mo_{10}$ (at.%) MPEA surface. Not only this work provides a clear vision of the thermal stability of the passive oxide film but it also confirms the possibility to generalize the applied approach to compositionally complex MPEA alloys.

2 | EXPERIMENTAL

2.1 | Sample preparation

Experiments were performed with a $Cr_{15}Fe_{10}Co_5Ni_{60}Mo_{10}$ (at.%) MPEA sample of single-phase *fcc* structure, denoted as MPEA-15Cr10Mo hereafter. The sample surface was prepared by mechanical polishing starting with 1,200 grade SiC paper and finishing with 0.25 µm diamond suspension, successively cleaned in ultrasonicated baths of acetone, ethanol, and deionized water (Merk Millipore, resistivity of 18.2 MΩ.cm) and dried by compressed air.

Electrochemical passivation was performed in a three-electrode cell consisting of a saturated mercury sulfate reference electrode (MSE, $E_{SHE} = E_{MSE} + 0.64$ V), a Pt wire counter electrode, and the alloy surface as working electrode, of which an area of 0.38 cm^2 (delimited by a Viton O-ring) was exposed to the solution. The potentiostat used was a VersaSTAT4 (AMETEK). Passivation was performed in an Ar-deaerated 0.05 M H_2SO_4 electrolyte prepared from ultrapure chemicals (VWR) and deionized water. After 15 min of stabilization at open circuit potential, the surface was passivated by stepping the potential to 0 V_{MSE} for 1 h. The passivation potential, corresponding to the middle of the passive range, was selected based on previous potentiodynamic polarization curves measured on the same MPEA-15Cr10Mo sample.[48]

The thermal stability of the passive oxide film was studied by heating the passivated sample under UHV (residual pressure of 10^{-8}–10^{-7} mbar during heating) in the preparation chamber of the XPS platform. To do so, the sample was heated up from room temperature (RT) to the target temperature and maintained at this temperature for a time period of 15 min. The temperature ramp rate was ~6°C/s. The tested temperatures were 100°C, 200°C, 300°C, 400°C, and 500°C. After each heating experiment, the sample was cooled down to RT and then transferred to the XPS analysis chamber for measurement. The highest tested temperature was 500°C at which the surface oxides were eliminated.

2.2 | XPS analytical conditions and spectral decomposition

XPS measurements were carried out in a Thermo Electron ESCALAB 250Xi spectrometer operating at a pressure of 10^{-9} mbar using a monochromatic Al Kα X-ray source (hν = 1,486.6 eV). High-resolution spectra of the Cr 2p, Fe 2p, Co 2p, Ni 2p, Mo 3d, S 2p, and C 1 s core levels were recorded at photoelectron take-off angle of 90°, with a pass energy of 20 eV and a step size of 0.1 eV.

The XPS analytical methodology based on the decomposition of the 3p core level spectral region (30–80 eV BE), previously proposed for the equimolar CrFeCoNiMn Cantor alloy[29] and $Al_xCoCrFeNi$ alloys,[7] could not be employed in the present work because of the weak intensities of Co, Fe, and Mo constituents, of lower concentration, 10, 5, and 10 at.%, respectively, than in the Cantor alloy. Instead, we applied the spectral decomposition methodology previously developed for this alloy and involving the subtraction of Auger peaks overlapping the 2p core level spectra.[49] The area of the Co $L_2M_{23}M_{45}$ and Ni $L_3M_{23}M_{45}$ Auger peaks overlapping the Fe 2p core level region was determined according to the corresponding $2p_{3/2}$ peak area and the reference Auger/$2p_{3/2}$ area ratios of 0.615 and 0.350 previously obtained for pure nickel for pure cobalt, respectively.

Data processing (curve fitting) was performed with CasaXPS applying a Shirley-type background subtraction. For Ni, only the Ni $2p_{3/2}$ spectral region was decomposed, while for Cr, Fe, Co, S, and

Mo, the entire 2p or 3d core level region was decomposed due to the overlaps between the $2p_{3/2}$-$2p_{1/2}$ or $3d_{5/2}$-$3d_{3/2}$ spin-orbit doublets. Constraints on Binding Energy (BE), Full Width at Half Maximum (FWHM), intensity ratio and splitting of spin-orbit doublets, and line shape were applied. For the metallic components, we used in-house reference line shapes, either fitted with LF (α, β, w, m) line shapes for representing the asymmetry or without detailed decomposition when more than two peaks were needed for fitting.[49] The LF (α, β, w, m) line

TABLE 1 Parameters and assignments of the component peaks obtained by XPS curve fitting for the passivated MPEA-15Cr10Mo surface before and after heating at different temperatures

Core level region	Peak assignment	BE ($s = +\frac{1}{2}$ /$s = -\frac{1}{2}$) (±0.1 eV)	FWHM ($s = +\frac{1}{2}$ /$s = -\frac{1}{2}$) (±0.1 eV)
Cr 2p	$Cr(0)_{met}$ (**A**: Cr $2p_{3/2}$)	574.0/A + 9.3 (RT-200 °C)	1.1/1.4 (RT, 100°C)
			1.1/1.6 (200°C)
		574.2/A + 9.3 (300–500°C)	1.4/1.9 (300°C)
			1.6/2 (400°C)
			1.2/1.8 (500°C)
	$Cr\ (III)_{ox}$	A + 2.7[a]	-[b]
	$Cr\ (III)_{hyd}$	A + 3.3/A + 13.0	2.6/2.6
Fe 2p	$Fe(0)_{met}$ (**B**: Fe $2p_{3/2}$)	707.0[a]	-[b]
	$Fe\ (II)_{ox/hyd}$	B + 2.4/B + 15.4	2.5/2.5
	$Fe\ (II)_{ox/hyd}$ satellite	B + 5.9/B + 19.2	3.7/3.7
	$Fe\ (III)_{ox/hyd}$	B + 4.1/B + 17.4	2.5/2.5
	$Fe\ (III)_{ox/hyd}$ satellite	B + 7.1/B + 20.4	4.2/4.2
	Ni $L_3M_{23}M_{45}$ Auger	D-140.4	-[b]
	Co $L_2M_{23}M_{45}$ Auger	C-65.4	-[b]
Co 2p	$Co(0)_{met}$	778.2[a]	-[b]
Ni $2p_{3/2}$	$Ni(0)_{met}$ (**C**: Ni $2p_{3/2}$)	852.8	0.8
	$Ni(0)_{met}$ satellite	C + 6.1 (RT-200°C)	3.0 (RT, 100°C)
		C + 6.3 (300°C)	2.8 (200°C)
		C + 6.5 (400°C, 500°C)	2.6 (300–500°C)
	$Ni\ (II)_{hyd}$	C + 3.3	2.0 (RT, 100°C)
			1.7 (200°C)
	$Ni\ (II)_{hyd}$ satellite	C + 8.8	3.3
Mo 3d	$Mo(0)_{met}$ (**D**: Mo $3d_{5/2}$)	227.8/D + 3.2 (RT-300°C)	0.6/0.7
		228.0/D + 3.2 (400, 500°C)	
	$Mo\ (III)_{ox}$	D + 0.7/D + 3.9	1.3/1.3
	$Mo\ (IV)_{ox}$	D + 1.4/D + 4.5	1.5/1.5
		D + 3.6/D + 6.8	2.0/2.0
	$Mo\ (VI)_{ox}$	D + 4.8/D + 8.0	1.3/1.3
S 2p	SO_4^{2-} (**E**: S $2p_{3/2}$)	168.8/E+1.3 (RT)	1.2/1.2
		169.0/E+1.3 (100–300°C)	
S 2 s	SO_4^{2-}	E+64.4	2.9
C 1 s	C-C, C-H (**F**)	285.0 (RT, 100°C)	1.5
		284.8 (200°C, 300°C)	
		284.6 (400°C, 500°C)	
	C-OH	F + 1.5	1.5
	C=O	F + 3.0	1.5
	O-C=O	F + 4.0	1.5
	CO_3^{2-}	F + 5.0	1.5
	Carbide	283.0 (500°C)	0.8 (500°C)

[a]No $2p_{1/2}$ component since the reference line shape measured on the pure substance was not decomposed in a doublet.
[b]The FWHM was fixed to that obtained for the reference line shape measured on the pure substance.

shape represents an asymmetric Lorentzian curve convoluted by a Gaussian curve, with α and β defining the spread of the Lorentzian tail of each side of the peak, w the damping of the tail, and m the width of the Gaussian. An in-house reference line shape was also used for Cr oxide to take into account its discrete structure resulting from multiplet splitting.[50] The other non-metallic peaks were fitted with symmetric Gaussian/Lorentzian line shape products GL(x) with x ranging from 0 to 100 and defining the percentage of Lorentzian character.

Similar to previous work, a $3d_{5/2}$-$3d_{3/2}$ doublet between the widely reported Mo (IV) and Mo (VI) doublets was detected and assigned to Mo (IV) in the present work.[49,51] For the sake of visibility, the two symmetric doublets of Mo (IV) are fused into an asymmetric one in the reported figures. After heating, BE shifts were observed for several components, which is also reported in the literature.[52] The C 1s spectra were decomposed to quantify adventitious carbon contaminations, thereby quantifying the oxygen contained in contamination species. Peak assignments, BE values, and FWHM values are compiled in Table 1.

3 | RESULTS

Figure 1 shows as examples the peak-fitted Cr 2p, Fe 2p, Co 2p, and Ni 2p spectra obtained after heating at 100°C and the Mo 3d spectrum obtained after heating at 300°C, the latter being chosen to illustrate the presence of the Mo (III) doublet. Ni (II) and Cr (III) hydroxide, Cr (III), Mo (IV), Mo (VI), and Mo (III) oxide and Fe (II), Fe (III), and Co (II) (hydr)oxide species were identified depending on temperature. The hydroxide species only exist below 300°C because of dehydroxylation. Mo (III) oxide, initially undetected at lower temperature, was identified after heating at 300°C and 400°C, with its 3d doublet located at 232.6–235.8 eV between metallic Mo(0) and oxidized Mo (IV).[53] The nature (oxide and/or hydroxide) of the Fe (II), Fe (III), and Co (II) species cannot be unambiguously determined due to the very weak intensities of the 2p component peaks compared to the overlapping Auger peaks.

Quantification of the passive oxide film composition and thickness was done after each heating step using a single-layer model of photoelectron intensity attenuation,[54] that is, considering abrupt,

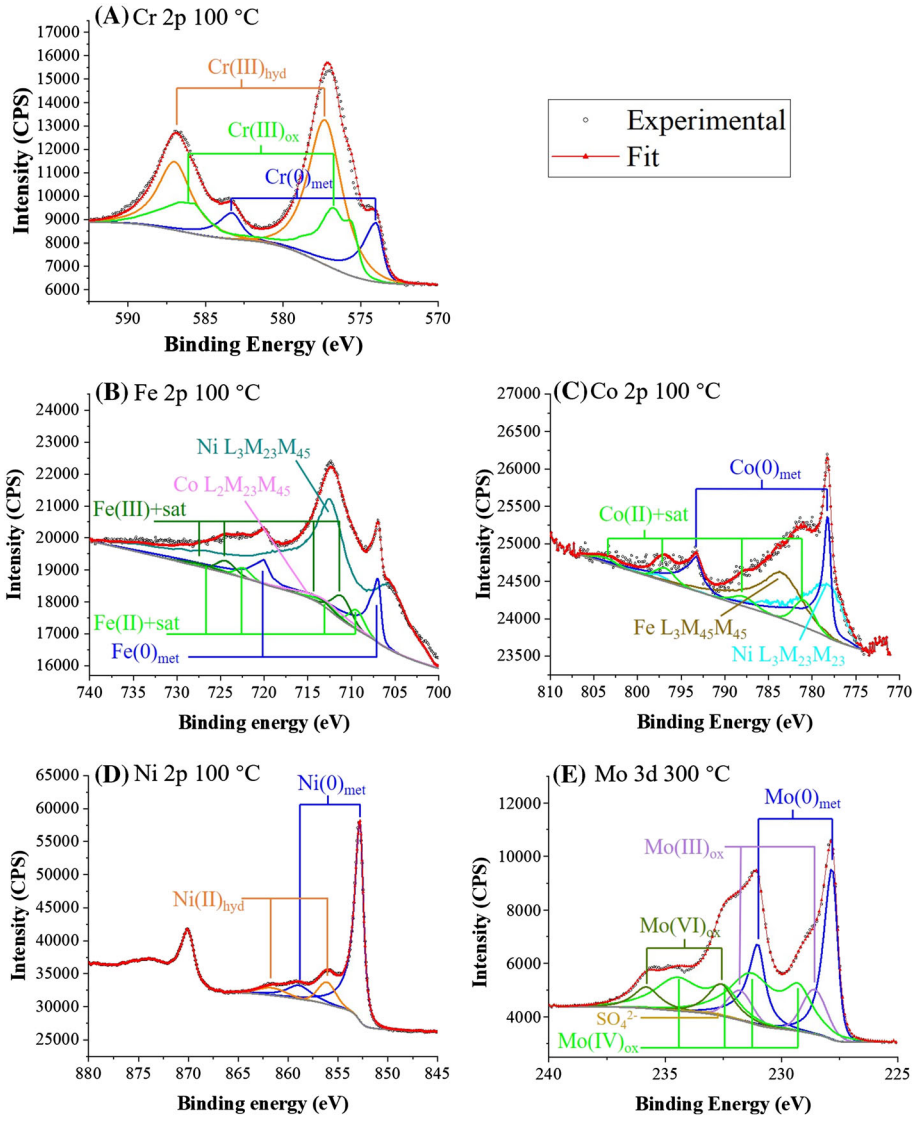

FIGURE 1 XPS spectral decomposition of the Cr 2p (A), Fe 2p (B), Co 2p (C), Ni 2p (D), and Mo 3d (E) core level regions for the MPEA-15Cr10Mo surface passivated at 0 V_{MSE} in 0.05 M H_2SO_4 for 1 h. (A–D) Obtained after heating at 100°C and (E) after heating at 300°C under UHV

non-diffuse metal/oxide/environment interfaces and a homogeneous in-depth distribution of the different species in the oxide layer. Thus, all identified oxidized components were attributed to the cations in the oxide film, whereas the metallic components were attributed to the alloy underneath. Values of the photoionization cross-section of each element for Al Kα emission at 1,486.6 eV were taken from Scofield,[55] and the inelastic mean free paths of the emitted photoelectrons were calculated according to Tanuma et al.[56] For each species, the intensities of the main and satellite peaks were taken into account for quantification since originating from the same measured orbital.[57] Ion densities (at·cm^{-3}) of each element were then calculated with an assumed oxide film density of 4.5 g·cm^{-3} and weighted by the oxide film thickness to obtain the surface ion density expressed in at·cm^{-2} and used to express the absolute variation of the amount of each species in the oxide film. The oxygen in adventitious carbon contamination, C-OH, C=O, O-C=O, and carbonate, was calculated and subtracted for quantification of the oxygen content of the oxide film according to the O/C stoichiometric ratios. Ion surface densities and film thickness are plotted in Figure 2 as a function of heating temperature.

Regarding oxygen, its content in the oxide film continuously decreases after UHV heat treatment at 100°C, 200°C, and 300°C. At 400°C, oxygen loss appears stopped, but it resumes when the temperature is increased to 500°C. In contrast to oxygen, the overall cation content of the oxide film remains rather stable up to 400°C but significantly drops at 500°C. Although the total quantity of cations does not change at 200°C, one observes the loss of Ni cations, whereas the quantity of the other cations slightly increases. At 300°C, Ni cations are no longer detected by XPS, and the decrease in Co cations is marked. The content in Co cations is very low throughout the whole sequence due to the low Co bulk content (5 at.%) in the substrate alloy; thus, the role of Co will not be further discussed. At 400°C, the Fe and Mo contents decrease, whereas the Cr content markedly increases. At 500°C, the Cr content drastically drops accompanying the loss of the other oxidized elements. The oxide film is eliminated. At this temperature of 500°C, the metallic surface underneath the residual oxide film becomes strongly enriched in Cr. The percentage of metallic Cr in the alloy raises sharply from 9–14 at.% for heat treatments up to 400°C to 25% after heating at 500°C. Besides, carbides are also detected after heating at 500°C, with a C/cations ratio of about 0.09.

Regarding Mo, previous work on this alloy has shown that Mo cations are present in different oxidation states, that is, Mo (IV) and Mo (VI), with a stratified in-depth distribution proposed to be at the origin of the enhanced passivity of this alloy.[49] An important feature of the present work is that new Mo species of lower valence (Mo (III)) are observed after heating at 300°C, indicating that Mo reduction occurs upon UHV heating. The evolution of the content in each Mo species in the oxide film is plotted in Figure 3. The content in Mo (VI) decreases after each heating step, first slowly at 100°C and then more rapidly at 200°C and above. At 500°C, Mo (VI) finally becomes undetectable. Concomitantly, Mo (IV) content continuously increases at 100°C and 200°C and then drops above 300°C until vanishing at 500°C. Mo (III), not initially present, is detected after heating at 300°C and decreases at higher temperature, becoming undetectable at 500°C.

4 | DISCUSSION

The above results allow us to discuss the overall mechanism of alterations of the passive oxide film induced by thermal heating under UHV (Figure 4). After heating at 100°C, the decrease in the oxygen surface density is not accompanied by any significant change in cation content or oxide film thickness. Besides, the O^{2-}/OH^{-} (O 1s spectrum not shown) and Cr_{ox}/Cr_{hyd} intensity ratios increase from 0.4 (RT) to 0.6 (100°C) and from 0.3 to 0.5, respectively. This indicates

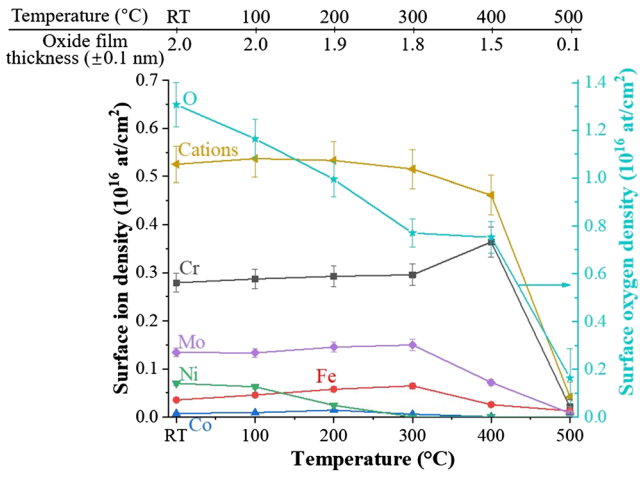

FIGURE 2 Oxide film thickness and surface densities in metal cations and oxygen for the passivated MPEA-15Cr10Mo surface before and after UHV heating at temperature up to 500°C. RT refers to room temperature.

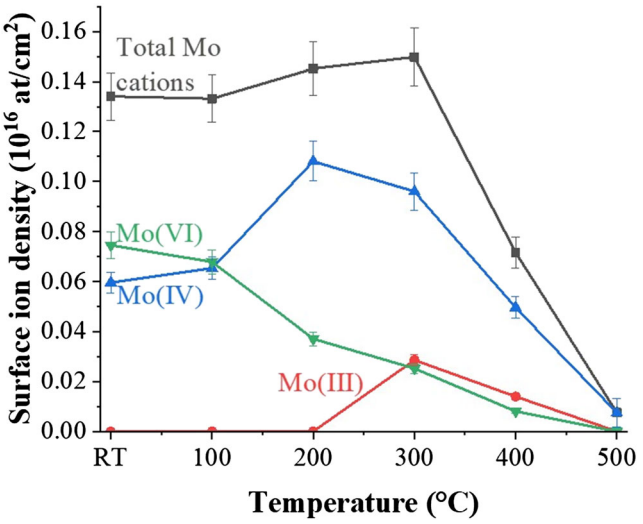

FIGURE 3 Surface densities of Mo cations of different chemical valence for the passivated MPEA-15Cr10Mo surface before and after UHV heating at temperature up to 500°C

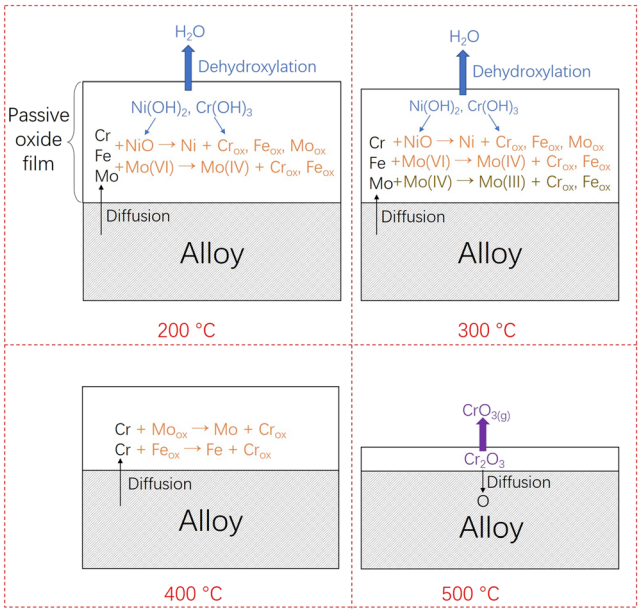

FIGURE 4 Alteration mechanisms of the passivated MPEA-15Cr10Mo surface upon vacuum heating

that, at this stage of thermally induced alteration, the passive film is mainly dehydrated and dehydroxylated, in agreement with dehydration and dehydroxylation of Ni hydroxide and Cr hydroxide that start below 100°C.[58,59] However, NiO, the product of Ni $(OH)_2$ dehydroxylation,[58,60] is not observed in our experiments, like in previous work on Ni-Cr alloys.[38] This suggests that NiO could be a transitory species immediately reduced to metallic Ni after formation, which is supported by the slight decrease of Ni cations. Thermodynamically, the reducing agents could be Cr, Fe, and Mo diffusing from the alloy since they all have lower Gibb's standard free energy of oxide formation than Ni.[61]

At 200°C, the surface density of oxygen continues to decrease. The O^{2-}/OH^{-} and Cr_{ox}/Cr_{hyd} ratios raise to 1.3 and 1.6, respectively. These changes suggest that the dehydration/dehydroxylation of the passive oxide film continues. At the same time, the loss of Ni cations attributed to dehydroxylation, and reduction is more marked. Regarding the amounts of Mo species, Mo (VI) decreases, while Mo (IV) increases, suggesting the reduction of Mo (VI) to Mo (IV) following the reaction: $2MoO_3 + Mo \rightarrow 3MoO_2$.[62] Thermodynamically, the reduction of Mo (VI) by Cr and Fe is also possible according to the Gibb's free energies of oxide formation. Assuming that all variations of the cation quantities are solely due to redox reactions, the charge gained by the reduced species and charge lost by the oxidized species are calculated to be 2.6 (±0.2) × 10^{15} e^{-}/cm^2 and 2.3 (±0.2) × 10^{15} e^{-}/cm^2, respectively, which balance confirms that redox reactions predominate the oxide film alteration.

At 300°C, the surface density of oxygen still decreases. The residual Ni cations disappear, and there is a remarkable raise in the Cr_{ox}/Cr_{hyd} ratio from 1.6 to 4.9, suggesting the complete reduction of Ni cations and advanced dehydroxylation of the passive oxide film, respectively. Although the total amount of Mo cations (Figure 2) remains unchanged, the surface density of both Mo (IV) and Mo (VI) cations decreases, while the lower Mo (III) oxidation state is identified (Figure 3), indicating that both Mo (IV) and Mo (VI) are reduced to Mo (III), likely by metallic Fe, Cr, and Mo. The diffusion of elements from the alloy into the oxide and the redox reactions may cause modifications of the physical surface/interface morphology and chemical environment and lead to the changes in the XPS peaks FWHM observed after heat treatment (Table 1). The possible formation of a tiny amount of suboxide such as CrO, and thus the presence of another minor oxide peak resulting in the observed apparent peak broadening, cannot be excluded.

Besides, at this temperature of 300°C, the charge calculations are clearly unbalanced with values of charge gained by the reduced species and charge lost by the oxidized species of 1.8 (±0.1) × 10^{15} e^{-}/cm^2 and 1.1 (±0.1) × 10^{15} e^{-}/cm^2, respectively. This unbalance suggests that the redox reactions were also accompanied by oxide volatilization or decomposition, possibly of Mo (VI) species.[62–64] It is also reasonable to suppose that the remaining Mo (IV) and Mo (VI) may subsist due to kinetic limitation and may be further or even totally removed by more prolonged heating.

At 400°C, the unchanged oxygen surface density confirms that the dehydroxylation is completed after cumulative heating up to 300°C. Referring to the Ellingham Diagram[61] and thermodynamic data,[65] the decrease in Fe cations and Mo cations and the increase in Cr cations may be due to the reduction of Mo oxides and Fe oxides by metallic Cr, accompanied by volatilization or decomposition of Mo species as suggested by the charge balance calculation, yielding a charge gain of 4.4 (±0.3) × 10^{15} e^{-}/cm^2 and a charge loss of 2.1 (±0.2) × 10^{15} e^{-}/cm^2. Consequently, UHV heating at 400°C results in a passive oxide film markedly more enriched in Cr (79 at.% Cr cations) compared to the initial oxide film formed at RT (53 at.% Cr cations).

At 500°C, the sharp drop in the quantity of all species indicates that the passive oxide film is unstable under UHV at this temperature. The tiny equivalent thickness of residual oxide (0.1 nm) suggests that the remaining oxide species should not form a fully covering layer. The instability of Cr oxide at moderate temperature under dry conditions has been reported in many works[38,39,66] and attributed to the reaction:

$$Cr_2O_{3(s)} + \frac{3}{2}O_{2(g)} \rightarrow 2CrO_{3(g)}. \quad (1)$$

In this work, considering the ultra-low oxygen partial pressure and the enrichment of metallic Cr after the elimination of Cr oxide, another $CrO_{3(g)}$ formation reaction is also suggested:

$$Cr_2O_{3(s)} \rightarrow Cr_{(s)} + CrO_{3(g)}. \quad (2)$$

Thermodynamically, at $p(O_{2(g)}) < 10^{-7}$ mbar, the theoretical $CrO_{3(g)}$ pressure needed to trigger reaction (1) is lower than 10^{-19} mbar, and that to trigger reaction (2) is even much lower, around 10^{-42} mbar, independently of the oxygen partial pressure. Although the thermodynamic thresholds to generate $CrO_{3(g)}$ are hard to reach,

the low bulk Cr concentration, the fact that the Cr oxide in the passive oxide film is not well crystallized,[39,67] and the redeposition of $CrO_{3(g)}$ in the form of Cr_2O_3[35,36] in the colder parts of the chamber may reduce the threshold of the reactions. The possibility of having Cr oxide reduction by residual reductive gas, for example, $H_{2(g)}$ or $CO_{(g)}$, cannot be excluded.

On a thermodynamic basis, Cr oxide elimination via decomposition can also be considered. Theoretically, the oxygen partial pressure to trigger the direct decomposition of $Cr_2O_{3(s)}$ to $Cr_{(s)}$ and $O_{2(g)}$ at 500°C is 10^{-40} atm, which is far lower than the residual pressure in our experiment. Moreover, no evident increase of O_2 partial pressure was detected during heating. Therefore, a decomposition mechanism driven by oxygen dissolution into bulk alloy towards the thermodynamic equilibrium of M-O system is considered. For an oxygen solubility of 0.1 at.% in the alloy,[68–70] the total oxygen decrease at 500°C would lead to the oxygen dissolution into the substrate alloy reaching about 860 nm in depth, which is too deep to be achieved with an oxygen diffusion coefficient lower than 10^{-13} $cm^2 \cdot s^{-1}$.[69,71,72] Thus, an oxide decomposition mechanism driven by oxygen diffusion into alloy is not excluded but cannot be the only mechanism of the oxide elimination observed at 500°C.

5 | CONCLUSION

Quantitative XPS analysis was applied to investigate the thermal stability under UHV of the protective oxide film formed by electrochemical passivation on *fcc* single-phase $Cr_{15}Fe_{10}Co_5Ni_{60}Mo_{10}$ (at.%) MPEA. A specific spectral decomposition methodology involving the subtraction of overlapping Auger peaks in the Fe 2p and Co 2p region was adopted for XPS curve fitting.

The results show that thermal heating at 100°C in UHV mainly leads to dehydration and dehydroxylation of the passive oxide film. Compositional alterations are observed after heating at 200°C and above. At 200°C, dehydroxylation and reduction of Ni hydroxide by elements diffusing from the alloy results in the loss of Ni (II) components without significant thinning of the oxide film. Reduction of Mo (VI) to Mo (IV) is also observed at 200°C, and further to Mo (III) at 300°C, together with slight volatilization or decomposition. At 400°C, Fe and Mo oxides are reduced by Cr diffusing from the alloy, causing the passive oxide film to become more strongly enriched in Cr (III) oxide than initially. At 500°C, the passive oxide film is unstable and eliminated, likely via the formation of volatile $CrO_{3(g)}$. Decomposition driven by oxygen diffusion from the surface oxide into the bulk alloy or reduction by residual reductive gas cannot be excluded.

This work shows also that stepwise in situ XPS analysis combined with thorough quantitative data exploitation is insightful to study the thermal stability of surface oxide films. The employed XPS spectral decomposition approach is not only proven to be appropriate for the studied MPEA but also enlightening for developing a generalized systematic decomposition methodology applicable to all MPEAs, which requires intensive reference XPS measurements and proper data processing.

ACKNOWLEDGMENT

This work was supported by the H2020 European Research Council (ERC) under the European Union's Horizon 2020 research and innovation programme (ERC Advanced Grant agreement No. 741123).

DATA AVAILABILITY STATEMENT

The data that support the findings of this study are available from the corresponding author upon reasonable request.

ORCID

Xueying Wang https://orcid.org/0000-0002-4967-8133

REFERENCES

1. Huang P-K, Yeh J-W, Shun T-T, Chen S-K. Multi-principal-element alloys with improved oxidation and wear resistance for thermal spray coating. *Adv Eng Mater*. 2004;6(12):74-78. doi:10.1002/adem.200300507
2. Cantor B, Chang ITH, Knight P, Vincent AJB. Microstructural development in equiatomic multicomponent alloys. *Mater Sci Eng A*. 2004;375-377:213-218. doi:10.1016/j.msea.2003.10.257
3. Birbilis N, Choudhary S, Scully JR, Taheri ML. A perspective on corrosion of multi-principal element alloys. *Npj Mater Degrad*. 2021;5(1):1-8, 14. doi:10.1038/s41529-021-00163-8
4. Lu P, Saal JE, Olson GB, et al. Computational materials design of a corrosion resistant high entropy alloy for harsh environments. *Scr Mater*. 2018;153:19-22. doi:10.1016/j.scriptamat.2018.04.040
5. Lu P, Saal JE, Olson GB, et al. Computational design and initial corrosion assessment of a series of non-equimolar high entropy alloys. *Scr Mater*. 2019;172:12-16. doi:10.1016/j.scriptamat.2019.07.003
6. Luo H, Li Z, Mingers AM, Raabe D. Corrosion behavior of an equiatomic CoCrFeMnNi high-entropy alloy compared with 304 stainless steel in sulfuric acid solution. *Corros Sci*. 2018;134:131-139. doi:10.1016/j.corsci.2018.02.031
7. Shi Y, Yang B, Xie X, Brechtl J, Dahmen KA, Liaw PK. Corrosion of Al_xCoCrFeNi high-entropy alloys: Al-content and potential scan-rate dependent pitting behavior. *Corros Sci*. 2017;119:33-45. doi:10.1016/j.corsci.2017.02.019
8. Li T, Swanson OJ, Frankel GS, et al. Localized corrosion behavior of a single-phase non-equimolar high entropy alloy. *Electrochim Acta*. 2019;306:71-84. doi:10.1016/j.electacta.2019.03.104
9. Strehblow H-H, Maurice V, Marcus P. Passivity of metals. In: Marcus P, ed. *Corrosion Mechanisms in Theory and Practice*. 3rd ed. CRC Press, Taylor and Francis; 2011:235-326.
10. Lim AS, Atrens A. ESCA studies of Ni-Cr alloys. *Appl Phys A*. 1992;54(4):343-349. doi:10.1007/BF00324199
11. Olefjord I, Wegrelius L. Surface analysis of passive state. *Corros Sci*. 1990;31:89-98. doi:10.1016/0010-938X(90)90095-M
12. Maurice V, Yang WP, Marcus P. X-ray photoelectron spectroscopy and scanning tunneling microscopy study of passive films formed on (100) Fe-18Cr-13Ni single-crystal surfaces. *J Electrochem Soc*. 1998;145(3):909-920. doi:10.1149/1.1838366
13. Quiambao KF, McDonnell SJ, Schreiber DK, et al. Passivation of a corrosion resistant high entropy alloy in non-oxidizing sulfate solutions. *Acta Mater*. 2019;164:362-376. doi:10.1016/j.actamat.2018.10.026
14. Dai C, Luo H, Li J, Du C, Liu Z, Yao J. X-ray photoelectron spectroscopy and electrochemical investigation of the passive behavior of high-entropy FeCoCrNiMo_x alloys in sulfuric acid. *Appl Surf Sci*. 2020;499:143903. doi:10.1016/j.apsusc.2019.143903
15. Wang Z, Di-Franco F, Seyeux A, Zanna S, Maurice V, Marcus P. Passivation-induced physicochemical alterations of the native surface

oxide film on 316L austenitic stainless steel. *J Electrochem Soc*. 2019;166(11):C3376-C3388. doi:10.1149/2.0321911jes

16. Marcus P, Olefjord I. A round Robin on combined electrochemical and AES/ESCA characterization of the passive films on Fe-Cr and Fe-Cr-Mo alloys. *Corros Sci*. 1988;28(6):589-602. doi:10.1016/0010-938X(88)90026-1
17. Ryan MP, Newman RC, Thompson GE. Atomically resolved STM of oxide film structures on Fe-Cr alloys during passivation in sulfuric acid solution. *J Electrochem Soc*. 1994;141(12):L164-L165. doi:10.1149/1.2059380
18. Castle JE, Qiu JH. A co-ordinated study of the passivation of alloy steels by plasma source mass spectrometry and x-ray photoelectron spectroscopy—1. Characterization of the passive film. *Corros Sci*. 1989;29(5):591-603. doi:10.1016/0010-938X(89)90010-3
19. Zhang X, Zagidulin D, Shoesmith DW. Characterization of film properties on the Ni-Cr-Mo alloy C-2000. *Electrochim Acta*. 2013;89:814-822. doi:10.1016/j.electacta.2012.11.029
20. Yu X, Gulec A, Sherman Q, et al. Nonequilibrium solute capture in passivating oxide films. *Phys Rev Lett*. 2018;121(14):145701. doi:10.1103/PhysRevLett.121.145701
21. Sherman QC, Voorhees PW, Marks LD. Thermodynamics of solute capture during the oxidation of multicomponent metals. *Acta Mater*. 2019;181:584-594. doi:10.1016/j.actamat.2019.09.043
22. Yu X-X, Perepezko JH, Marks LD. Crystallographic anisotropy of nonequilibrium solute capture. *Acta Mater*. 2020;198:223-229. doi:10.1016/j.actamat.2020.07.059
23. Yamamoto T, Fushimi K, Seo M, Tsuri S, Adachi T, Habazaki H. Depassivation–repassivation behavior of type-312L stainless steel in NaCl solution investigated by the micro-indentation. *Corros Sci*. 2009;51(7):1545-1553. doi:10.1016/j.corsci.2008.11.020
24. Vignal V, Olive JM, Desjardins D. Effect of molybdenum on passivity of stainless steels in chloride media using ex situ near field microscopy observations. *Corros Sci*. 1999;41(5):869-884. doi:10.1016/S0010-938X(98)00155-3
25. Maurice V, Peng H, Klein LH, Seyeux A, Zanna S, Marcus P. Effects of molybdenum on the composition and nanoscale morphology of passivated austenitic stainless steel surfaces. *Faraday Discuss*. 2015;180:151-170. doi:10.1039/C4FD00231H
26. Newman RC. The dissolution and passivation kinetics of stainless alloys containing molybdenum—1. Coulometric studies of Fe Cr and Fe Cr Mo alloys. *Corros Sci*. 1985;25(5):331-339. doi:10.1016/0010-938X(85)90111-8
27. Lloyd AC, Noël JJ, McIntyre S, Shoesmith DW. Cr, Mo and W alloying additions in Ni and their effect on passivity. *Electrochim Acta*. 2004;49(17-18):3015-3027. doi:10.1016/j.electacta.2004.01.061
28. Marcus P, Moscatelli M. The role of alloyed molybdenum in the dissolution and the passivation of nickel-molybdenum alloys in the presence of adsorbed sulfur. *J Electrochem Soc*. 1989;136(6):1634-1637. doi:10.1149/1.2096984
29. Wang L, Mercier D, Zanna S, et al. Study of the surface oxides and corrosion behaviour of an equiatomic CoCrFeMnNi high entropy alloy by XPS and ToF-SIMS. *Corros Sci*. 2020;167:108507. doi:10.1016/j.corsci.2020.108507
30. Castle JE, Ke R, Watts JF. Additional in-depth information obtainable from the energy loss features of photoelectron peaks: the oxidation and reduction of an Fe/Cr alloy in oxygen at low partial pressures and ultra high vacuum. *Corros Sci*. 1990;30(8-9):771-798. doi:10.1016/0010-938X(90)90002-M
31. Asteman H, Svensson J-E, Johansson L-G. Evidence for chromium evaporation influencing the oxidation of 304L: the effect of temperature and flow rate. *Oxidat Metals*. 2002;57:193-216. doi:10.1023/A:1014877600235
32. Stanislowski M, Wessel E, Hilpert K, Markus T, Singheiser L. Chromium vaporization from high-temperature alloys: I. Chromia-forming steels and the influence of outer oxide layers. *J Electrochem Soc*. 2007;154(4):A295. doi:10.1149/1.2434690
33. Franco FD, Seyeux A, Zanna S, Maurice V, Marcus P. Effect of high temperature oxidation process on corrosion resistance of bright annealed ferritic stainless steel. *J Electrochem Soc*. 2017;164(13):C869-C880. doi:10.1149/2.1851713jes
34. Tapping RL, Davidson RD, McAlpine E, Lister DH. The composition and morphology of oxide films formed on type 304 stainless steel in lithiated high temperature water. *Corros Sci*. 1986;26(8):563-576. doi:10.1016/0010-938X(86)90024-7
35. Caplan D, Cohen M. The volatilization of chromium oxide. *J Electrochem Soc*. 1961;108(5):438. doi:10.1149/1.2428106
36. Wang K, Dreger LH, Dadape VV, Margrave JL. Sublimation of Cr_2O_3 at high temperatures. *J Am Ceramic Soc (US)*. 1960;43(10):509-510. doi:10.1111/j.1151-2916.1960.tb13604.x
37. Wang L, Seyeux A, Marcus P. Thermal stability of the passive film formed on 316L stainless steel surface studied by ToF-SIMS. *Corros Sci*. 2020;165:108395. doi:10.1016/j.corsci.2019.108395
38. Wang Z, Carrière C, Seyeux A, Zanna S, Mercier D, Marcus P. Thermal stability of surface oxides on nickel alloys (NiCr and NiCrMo) investigated by XPS and ToF-SIMS. *Appl Surf Sci*. 2022;576:151836. doi:10.1016/j.apsusc.2021.151836
39. Poulain C, Seyeux A, Voyshnis S, Marcus P. Volatilization and transport mechanisms during Cr oxidation at 300°C studied in situ by ToF-SIMS. *Oxid Met*. 2017;88(3-4):423-433. doi:10.1007/s11085-017-9756-y
40. Wang L, Seyeux A, Perriere L, Mercier D, Maurice V, Marcus P. Insight on passivity of high entropy alloys: thermal stability and ion transport mechanisms in the passive oxide film on CoCrFeMnNi surfaces. *Corros Sci*. 2021;188:109540. doi:10.1016/j.corsci.2021.109540
41. Backman L, Opila EJ. Thermodynamic assessment of the group IV, V and VI oxides for the design of oxidation resistant multi-principal component materials. *J Eur Ceram Soc*. 2019;39(5):1796-1802. doi:10.1016/j.jeurceramsoc.2018.11.004
42. Backman L, Gild J, Luo J, Opila EJ. Part I: theoretical predictions of preferential oxidation in refractory high entropy materials. *Acta Mater*. 2020;197:20-27. doi:10.1016/j.actamat.2020.07.003
43. Nisar A, Sakthivel T, Zhang C, Boesl B, Seal S, Agarwal A. Quantification of complex protective surface oxide layer formed during plasma jet exposure of multicomponent ultra-high temperature carbides. *Appl Surf Sci*. 2022;592:153247. doi:10.1016/j.apsusc.2022.153247
44. Huang C, Zhang Y, Shen J, Vilar R. Thermal stability and oxidation resistance of laser clad TiVCrAlSi high entropy alloy coatings on Ti–6Al–4V alloy. *Surf Coat Technol*. 2011;206(6):1389-1395. doi:10.1016/j.surfcoat.2011.08.063
45. Newman RC. The dissolution and passivation kinetics of stainless alloys containing molybdenum—II. Dissolution kinetics in artificial pits. *Corros Sci*. 1985;25(5):341-350. doi:10.1016/0010-938X(85)90112-X
46. Shang X-L, Wang Z-J, Wu Q-F, Wang J-C, Li J-J, Yu J-K. Effect of Mo addition on corrosion behavior of high-entropy alloys $CoCrFeNiMo_x$ in aqueous environments. *Acta Metall Sin (Engl Lett)*. 2019;32(1):41-51. doi:10.1007/s40195-018-0812-7
47. Rodriguez AA, Tylczak JH, Gao MC, et al. Effect of molybdenum on the corrosion behavior of high-entropy alloys $CoCrFeNi_2$ and $CoCrFeNi_2Mo_{0.25}$ under sodium chloride aqueous conditions. *Adv Mater Sci Eng*. 2018;2018:1-11. doi:10.1155/2018/3016304
48. Wang X, Mercier D, Danard Y, et al. Enhanced passivity of Cr-Fe-co-Ni-Mo multi-component single-phase face-centred cubic alloys: design, production and corrosion behaviour. *Corros Sci*. 2022;200:110233. doi:10.1016/j.corsci.2022.110233
49. Wang X, Mercier D, Zanna S, et al. Origin of enhanced passivity of Cr-Fe-Co-Ni-Mo multi-principal element alloy surfaces. *Npj Mater Degrad*. Forthcoming.

50. Zanna S, Mercier D, Gardin E, Allion-Maurer A, Marcus P. EPS for bacterial anti-adhesive properties investigated on a model metal surface. *Colloids Surf B Biointerfaces*. 2022;213:112413. doi:10.1016/j.colsurfb.2022.112413
51. Scanlon DO, Watson GW, Payne DJ, Atkinson GR, Egdell RG, Law DSL. Theoretical and experimental study of the electronic structures of MoO_3 and MoO_2. *J Phys Chem C*. 2010;114(10):4636-4645. doi:10.1021/jp9093172
52. Biesinger MC, Brown C, Mycroft JR, Davidson RD, McIntyre NS. X-ray photoelectron spectroscopy studies of chromium compounds. *Surf Interface Anal*. 2004;36(12):1550-1563. doi:10.1002/sia.1983
53. Bjornsson R, Lima FA, Spatzal T, et al. Identification of a spin-coupled Mo (III) in the nitrogenase iron–molybdenum cofactor. *Chem Sci*. 2014;5(8):3096-3103. doi:10.1039/C4SC00337C
54. Jabs T, Borthen P, Strehblow H-H. X-ray photoelectron spectroscopic examinations of electrochemically formed passive layers on Ni-Cr alloys. *J Electrochem Soc*. 1997;144(4):1231-1243. doi:10.1149/1.1837577
55. Scofield JH. Hartree-Slater subshell photoionization cross-sections at 1254 and 1487 eV. *J Electron Spectrosc Relat Phenom*. 1976;8(2):129-137. doi:10.1016/0368-2048(76)80015-1
56. Tanuma S, Powell CJ, Penn DR. Calculations of electron inelastic mean free paths. II. Data for 27 elements over the 50–2000 eV range. *Surf Interface Anal*. 1991;17(13):911-926. doi:10.1002/sia.740171304
57. Brundle CR, Crist BV. X-ray photoelectron spectroscopy: a perspective on quantitation accuracy for composition analysis of homogeneous materials. *J Vac Sci Technol A*. 2020;38(4):041001. doi:10.1116/1.5143897
58. Ramesh TN. X-ray diffraction studies on the thermal decomposition mechanism of nickel hydroxide. *J Phys Chem B*. 2009;113(39):13014-13017. doi:10.1021/jp906578u
59. Huang Z, Chen C, Xie J, Wang Z. The evolution of dehydration and thermal decomposition of nanocrystalline and amorphous chromium hydroxide. *J Anal Appl Pyrolysis*. 2016;118:225-230. doi:10.1016/j.jaap.2016.02.006
60. Carney CS, Chinn RE, Doğan ÖN, Gao MC. Isothermal decomposition kinetics of nickel (II) hydroxide powder. *J Alloys Compd*. 2015;644:968-974. doi:10.1016/j.jallcom.2015.03.256
61. Ellingham HJT. Reducibility of oxides and sulphides in metallurgical processes. *J Soc Chem Ind*. 1944;125-133.
62. Gulbransen EA, Andrew KF, Brassart FA. Oxidation of molybdenum 550° to 1700°C. *J Electrochem Soc*. 1963;110(9):952. doi:10.1149/1.2425918
63. Lv X, Wang S, Gong L, et al. In-situ investigation on the thermal decomposition of van der Waals MoO_3. *Chem Phys Lett*. 2021;779:138840. doi:10.1016/j.cplett.2021.138840
64. Blackburn PE, Hoch M, Johnston HL. The vaporization of molybdenum and tungsten oxides. *J Phys Chem B*. 1958;62(7):769-773. doi:10.1021/j150565a001
65. Barin I. *Thermochemical Data of Pure Substances*. 3rd ed. Weinheim: VCH Verlagsgesellschaft mbH; 1995. doi:10.1021/ja965624c
66. Li Z, He Y, Gao W. Use of a solid-state oxygen pump to study oxidation kinetics of Cr and Mo. *Oxidat Met*. 2000;53:577-596. doi:10.1023/A:1004641328140
67. Maurice V, Marcus P. Progress in corrosion science at atomic and nanometric scales. *Progr Mater Sci*. 2018;95:132-171. doi:10.1016/j.pmatsci.2018.03.001
68. Kjellqvist L, Selleby M, Sundman B. Thermodynamic modelling of the Cr–Fe–Ni–O system. *Cal*. 2008;32(3):577-592. doi:10.1016/j.calphad.2008.04.005
69. Park J-W, Altstetter CJ. The diffusion and solubility of oxygen in solid nickel. *Metall Mater Trans A*. 1987;18(1):43-50. doi:10.1007/BF02646220
70. Aleksandrov AA, Dashevskii VY. Thermodynamics of the oxygen solutions in chromium-containing Ni–Co melts. *Russ Metall*. 2016;2016(7):642-648. doi:10.1134/S003602951607003X
71. Chattopadhyay B, Wood GC. The transient oxidation of alloys. *Oxid Met*. 1970;2(4):373-399. doi:10.1007/BF00604477
72. Perusin S, Monceau D, Andrieu E. Investigations on the diffusion of oxygen in nickel at 1000°C by SIMS analysis. *J Electrochem Soc*. 2005;152(12):E390. doi:10.1149/1.2116787

How to cite this article: Wang X, Mercier D, Zanna S, et al. XPS study of the thermal stability of passivated NiCrFeCoMo multi-principal element alloy surfaces. *Surf Interface Anal*. 2023;1-9. doi:10.1002/sia.7193